

Article

# Comparison of C14- and C15-Predominated $\text{AB}_2$ Metal Hydride Alloys for Electrochemical Applications

Kwo-Hsiung Young <sup>1,2,\*</sup> , Jean Nei <sup>2</sup> , Chubin Wan <sup>3,4</sup>, Roman V. Denys <sup>3</sup>  
and Volodymyr A. Yartys <sup>3,5</sup>

<sup>1</sup> Department of Chemical Engineering and Materials Science, Wayne State University, Detroit, MI 48202, USA

<sup>2</sup> BASF/Battery Materials—Ovonic, 2983 Waterview Drive, Rochester Hills, MI 48309, USA; jean.nei@basf.com

<sup>3</sup> Institute for Energy Technology, P.O. Box 40, NO-2027 Kjeller, Norway; cbinwan@gmail.com (C.W.); roman.v.denys@gmail.com (R.V.D.); volodymyr.yartys@ifet.no (V.A.Y.)

<sup>4</sup> Department of Physics, University of Science and Technology Beijing, Beijing 100083, China

<sup>5</sup> Department of Materials Science and Engineering, Norwegian University of Science and Technology, NO-7491 Trondheim, Norway

\* Correspondence: kwo.young@basf.com; Tel.: +1-248-293-7000

Academic Editor: Catia Arbizzani

Received: 24 May 2017; Accepted: 11 July 2017; Published: 28 July 2017

**Abstract:** Herein, we present a comparison of the electrochemical hydrogen-storage characteristics of two state-of-art Laves phase-based metal hydride alloys ( $\text{Zr}_{21.5}\text{Ti}_{12.0}\text{V}_{10.0}\text{Cr}_{7.5}\text{Mn}_{8.1}\text{Co}_{8.0}\text{Ni}_{32.2}\text{Sn}_{0.3}\text{Al}_{0.4}$  vs.  $\text{Zr}_{25.0}\text{Ti}_{6.5}\text{V}_{3.9}\text{Mn}_{22.2}\text{Fe}_{3.8}\text{Ni}_{38.0}\text{La}_{0.3}$ ) prepared by induction melting and hydrogen decrepitation. The relatively high contents of lighter transition metals (V and Cr) in the first composition results in an average electron density below the C14/C15 threshold ( $e/a \sim 6.9$ ) and produces a C14-predominated structure, while the average electron density of the second composition is above the C14/C15 threshold and results in a C15-predominated structure. From a combination of variations in composition, main phase structure, and degree of homogeneity, the C14-predominated alloy exhibits higher storage capacities (in both the gaseous phase and electrochemical environment), a slower activation, inferior high-rate discharge, and low-temperature performances, and a better cycle stability compared to the C15-predominated alloy. The superiority in high-rate dischargeability in the C15-predominated alloy is mainly due to its larger reactive surface area. Annealing of the C15-predominated alloy eliminates the ZrNi secondary phase completely and changes the composition of the La-containing secondary phase. While the former change sacrifices the synergetic effects, and degrades the hydrogen storage performance, the latter may contribute to the unchanged surface catalytic ability, even with a reduction in total volume of metallic nickel clusters embedded in the activated surface oxide layer. In general, the C14-predominated alloy is more suitable for high-capacity and long cycle life applications, and the C15-predominated alloy can be used in areas requiring easy activation, and better high-rate and low-temperature performances.

**Keywords:** metal hydride; nickel metal hydride battery; Laves phase alloy; electrochemistry; synergetic effect

## 1. Introduction

Nickel/metal hydride (Ni/MH) rechargeable batteries are widely used in today's consumer electronics, stationary power storage, and transportation applications. One of the major factors limiting the performance of Ni/MH batteries is a relatively low gravimetric energy density, compared to the rival lithium-ion battery technology [1]. For the active materials in the negative electrode of Ni/MH battery, Laves phase-based  $\text{AB}_2$  metal hydride (MH) alloy containing 1.85 wt % H with a potential capacity of  $434 \text{ mAh} \cdot \text{g}^{-1}$  [2] has commonly been a high-energy alternative to the conventional rare

earth-based  $\text{AB}_5$  alloys, which have a capacity of approximately  $330 \text{ mAh}\cdot\text{g}^{-1}$ . Other performance comparisons between these two MH alloy families are available in an earlier review article [3]. Different from the single  $\text{CaCu}_5$  crystal structure in the  $\text{AB}_5$  MH alloys, the main phase in the  $\text{AB}_2$  MH alloys can be C14, C15, or a mixture of two, which provides additional freedom in composition design to address various requirements, such as ultra-low temperature performance, high-temperature storage, and overcharge performance [4]. C14 and C15 are two Laves structures and form the largest intermetallic compound group [5].

The difference between these two structures originates from the different types of packings in two types of metal nets, Kagome 6363 nets formed by B atoms and containing hexagons and triangles, and  $\text{A}_2\text{B}$  buckled nets formed by both A and B atoms [6]. There are 6 types of these nets, depending on their orientation along the [001] direction of the hexagonal/trigonal unit cells, as shown in Figure 1; A, B, and C nets for the Kagome 6363 nets and a, b, and c nets for the  $\text{A}_2\text{B}$  buckled nets. The packing of these nets creates  $\text{AcBc}$  2-layer stacking, resulting in a hexagonal C14 type Laves type structure, or 3-layer stacking ( $\text{AcBaCb}$ ), resulting in a face-centered cubic (fcc) C15 Laves type structure, both with  $\text{AB}_2$  stoichiometry. As shown in Figure 1, atoms in the A layer form a triangular net and there are two possible arrangements for the next layer—atoms in the B or C position. If the stacking of the triangular nets follows the sequence A-B-A-B, as shown in Figure 1b, a hexagonal crystal structure is formed. In the case of another stacking sequence, A-B-C-A-B-C, the structure is fcc with the same packing density as for the hexagonal one (Figure 1c). For the Laves phases, the triangular net is replaced by an  $\text{A}_4\text{B}_8$  slab with an  $\text{A}_2\text{B}-\text{B}_3-\text{A}_2\text{B}-\text{B}_3$  structure, and C14 and C15 are formed following the A-B-A-B and A-B-C-A-B-C stacking sequences, respectively. Another member of the Laves phases, hexagonal C36, has the same building slabs, but they are stacked in a different sequence,  $\text{AbCaBaCb}$ . However, the C36 type of structure is much less abundant than C14 and C15 [7], and we will not discuss it further in this work.

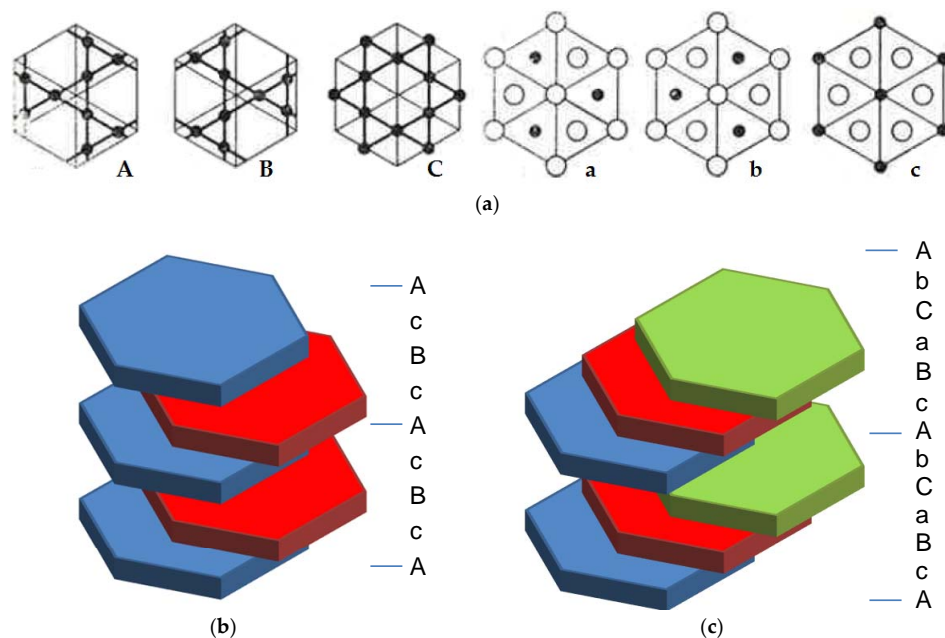


**Figure 1.** Stacking (a) units of each layer, (b) C14, and (c) C15 Laves type structures.

Figure 2 shows the crystal structures of C14 and C15 type alloys, and Table 1 summarizes the crystallographic data for both structures. Ideally, the lattice parameters are closely related in each structure and between structures. However, in the actual C14-predominated MH alloys, the  $c/a$  ratio is slightly lower than the theoretical value ( $2\sqrt{\frac{2}{3}} \cong 1.633$ ) [8,9]. Three types of positions are available for hydrogen occupation tetrahedral sites ( $\text{A}_2\text{B}_2$ ,  $\text{AB}_3$ , and  $\text{B}_4$ ) in both C14 and C15 structures, as shown in

Figure 2. In the Laves phases, octahedral sites are not present at all, therefore the following discussion will only concentrate on tetrahedral sites.

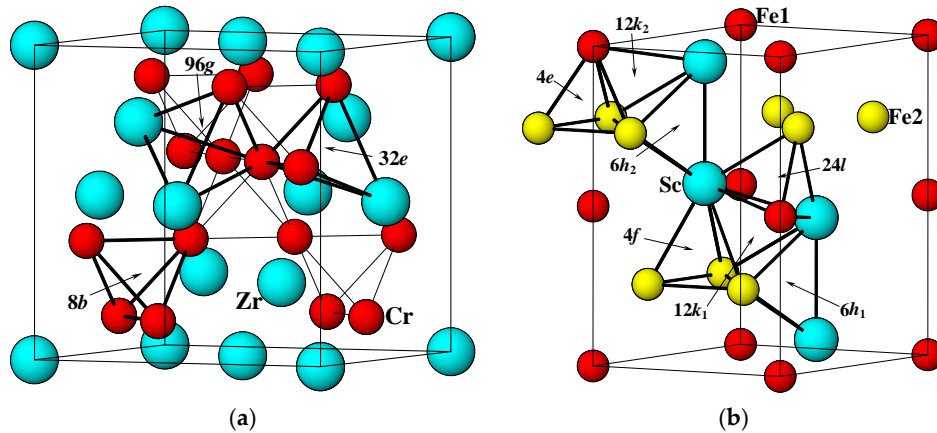


**Figure 2.** Unit cells for (a)  $\text{ZrCr}_2$  (C15) and (b)  $\text{ScFe}_2$  (C14) structures. Various tetrahedral hydrogen occupation sites ( $\text{A}_2\text{B}_2$ ,  $\text{AB}_3$ , and  $\text{B}_4$ ) are indicated by arrows.

**Table 1.** Basic physical parameters of C14 and C15. H-site denotes hydrogen occupying site.

Parameter	C14	C15
Crystal symmetry	Hexagonal ( $hP12$ )	Face-centered-cubic ( $cF24$ )
Space group	$P6_3/mmc$	$F\bar{d}3m$
Ideal lattice constant $a$	$a_{\text{C14}}$	$\sqrt{2}a_{\text{C14}}$
Ideal lattice constant $c$	$2\sqrt{\frac{2}{3}}a_{\text{C14}}$	-
Number of $\text{A}_2\text{B}_2$ /Full unit cell $\text{AB}_2$ tetrahedral H-sites per formula [10]	$12 (6h_1 + 6h_2 + 12k_1 + 24l)$	$12 (96g)$
Number of $\text{AB}_3$ tetrahedral H-site per formula [10]	$4 (4f + 12k_2)$	$4 (32e)$
Number of $\text{B}_4$ tetrahedral H-site per formula [10]	$1 (4e)$	$1 (8b)$
Maximum H-storage	Up to 5.4 at. H/ $\text{AB}_2$ [11]	Up to 7 at. H/ $\text{AB}_2$ [12]
Theoretical maximum H-storage	6.33 per $\text{AB}_2$ [13]	7 per $\text{AB}_2$ [13]

Hydrogen occupation occurs first at the  $\text{A}_2\text{B}_2$  site, next at the  $\text{AB}_3$  site, and finally at the  $\text{B}_4$  site [14–17]. Furthermore, the ratio between the tetrahedral sites is 12  $\text{A}_2\text{B}_2$ , 4  $\text{AB}_3$ , and 1  $\text{B}_4$  for both C14 and C15 structures. However, not all these sites can be occupied at the same time as the sites with a common triangular face are blocked from simultaneous occupancy. This is because the distance between their centers appears to be well below 0.2 nm, the minimum allowed H-H distance in the structures of metal hydrides [18].

Storages of up to 5.4 and 4.25 H atoms per  $\text{AB}_2$  formula unit for the C14 and C15 structures, respectively, have been demonstrated at room temperature and in a reasonable pressure range, although their theoretical hydrogen storage (H-storage) capacities are higher (6.33 and 6 H atoms per  $\text{AB}_2$  formula unit for C14 and C15, respectively).

The choice of the dominating Laves structure at room temperature is not random. While several determining factors, such as atomic size ratio, difference in electronegativity between the A-site and B-site atoms [19], and stoichiometry [20] have been discussed in literature, average electron density ( $e/a$ ) was found to be the most crucial parameter and can be directly correlated to the ratio of C14/C15 at room temperature [21]. An empirical model for predicing the C14/C15 formation was originally supported by a set of tight-binding calculations [22] and recently confirmed by a density function theory calculation [23]. In addition, the model for  $e/a$  at the C14/C15 threshold (C14:C15 = 1:1) was further improved to include the contribution from the A-site atoms by incorporating the average chemical potential of the A-site atoms [24].

While the initial studies of the  $\text{AB}_2$  MH alloys in the gaseous phase [25] and electrochemical environment [26] started and were later commercialized with the C14 phase [3], studies on the C15-predominated  $\text{AB}_2$  alloys for Ni/MH application were common from 1991 to 2004. The major accomplishments during this period are summarized in Table 2. In order to increase the stability of the C15 phase, these alloys are generally designed to have a higher Zr-content (which moves  $e/a$  at the C14/C15 threshold to a lower value [27]), lower the V- and Cr-content (which increases  $e/a$  to a value above the  $e/a$  of the C14/C15 threshold [27]), and have a hyperstoichiometry ( $B/A > 2$ ), compared to the C14-predominated MH alloys used in Ni/MH applications. Although the C15 alloys that exhibit a high capacity and excellent high-rate dischargeability (HRD) have been successfully developed, they are not as popular as the C14 alloys. Through the years, the performance of the C14 and C15 phases in both the gaseous phase and electrochemical environment have been compared over a dozen times either in the alloys with the same composition but different preparation processes, or in a series of alloys with close compositions. Unfortunately, the findings are inconsistent (Table 3). It is very difficult to determine which phase has better performance with regard to capacity, HRD, and cycle life. In this paper, we provide a different approach to compare these two Laves structures. To this end, two state-of-art C14 and C15-based MH alloys were selected and their gaseous and electrochemical H-storages were compared. We hope this work would illuminate future  $\text{AB}_2$  MH alloy research.

**Table 2.** Summary of previous studies on the hydrogen storage properties of C15-predominated MH alloys in an electrochemical environment. AM, Ann, PM, LM, IM denote arc melting, annealing, plasma melting, levitation melting, and induction melting preparation methods, respectively.  $C_m$  is the discharge capacity obtained with an  $m \text{ mA}\cdot\text{g}^{-1}$  discharge current. HRD and EC are abbreviations for high-rate dischargeability and electrochemistry, respectively.

Basic Composition	Preparation Method	Major Achievements	References	Year
$\text{ZrCr}_{0.4}\text{Mn}_{0.4}\text{Ni}_{1.2}$	AM + Ann	$C_{30}$ of $\sim 320 \text{ mAh}\cdot\text{g}^{-1}$	[28]	1991
$\text{ZrV}_{0.8}\text{Mn}_{0.4}\text{Ni}_{1.2}$	Ar PM	$C_{10}$ of $\sim 366 \text{ mAh}\cdot\text{g}^{-1}$	[29]	1991
$\text{ZrV}_{0.5}\text{Ni}_{1.5}$	LM	$C_{100}$ of $\sim 365 \text{ mAh}\cdot\text{g}^{-1}$	[30,31]	1994
$\text{ZrV}_{0.05}\text{Cr}_{0.25}\text{Mn}_{0.6}\text{Ni}_{1.3}$	AM	$C_{50}$ of $343 \text{ mAh}\cdot\text{g}^{-1}$	[32]	1995
$\text{ZrV}_{0.5}\text{Mn}_{0.5}\text{NiMo}_{0.15}$	AM	$C_{50}$ of $339 \text{ mAh}\cdot\text{g}^{-1}$	[33]	1995
$\text{ScCr}_{0.2}\text{Mn}_{0.5}\text{Co}_{0.2}\text{Ni}_{1.1}$	AM	$C_{70}$ of $400 \text{ mAh}\cdot\text{g}^{-1}$	[34]	1995
$\text{ZrV}_{0.33}\text{Mn}_{0.86}\text{Co}_{0.11}\text{Ni}_{0.9}$	AM	$C_{17}$ of $440 \text{ mAh}\cdot\text{g}^{-1}$	[35]	1995
$\text{ZrV}_{1.5}\text{Ni}_{1.5}$	LM	$C_2$ of $800 \text{ mAh}\cdot\text{g}^{-1}$	[36]	1997
$\text{ZrV}_{0.2}\text{Cr}_{0.1}\text{Mn}_{0.6}\text{Ni}_{1.2}$	IM + Ann	$C_{80}$ of $330 \text{ mAh}\cdot\text{g}^{-1}$	[37]	1997
$\text{ZrV}_{0.5}\text{Mn}_{0.7}\text{Ni}_{1.2}$	AM	$C_{100}$ of $330 \text{ mAh}\cdot\text{g}^{-1}$	[38]	1998
$\text{ZrMn}_{1-x}\text{V}_x\text{Ni}_{1.4+y}$	AM	Surface area dominates EC performance	[39]	1998
$\text{ZrV}_{0.2}\text{Cr}_{0.05}\text{Mn}_{0.6}\text{Co}_{0.05}\text{Ni}_{1.2}$	IM + Ann	$C_{70}$ of $370 \text{ mAh}\cdot\text{g}^{-1}$	[40,41]	1998
$\text{ZrV}_{1.5}\text{Ni}_{1.5}$	IM	$C_{160}$ of $356 \text{ mAh}\cdot\text{g}^{-1}$	[42]	1999
$\text{Zr}(\text{VMnCoNi})_{2+\alpha}$	IM	300 cycle with stable capacity $C_{60} = 342 \text{ mAh}\cdot\text{g}^{-1}$	[43]	1999
$\text{Zr}_{0.5}\text{Ti}_{0.5}\text{V}_{0.6}\text{Mn}_{0.2}\text{Pd}_{0.1}\text{Ni}_{0.8}\text{Fe}_{0.2}$	AM	$C_{50}$ of $372 \text{ mAh}\cdot\text{g}^{-1}$	[44]	1999
$\text{ZrV}_{0.2}\text{Mn}_{0.6}\text{Cr}_{0.1}\text{Ni}_{1.2}$	AM	F-treatment with Ni improves cycle life	[45]	1999
$\text{Zr}_{0.4}\text{Ti}_{0.6}\text{V}_{1.2}\text{Cr}_{0.3}\text{Ni}_{1.5}$	AM	200 cycle with stable capacity	[46]	2000
$\text{ZrV}_{0.2}\text{Mn}_{0.6}\text{Co}_{0.1}\text{Ni}_{1.2}$	AM + Ann	$C_{50}$ of $\sim 350 \text{ mAh}\cdot\text{g}^{-1}$	[47]	2000
$\text{ZrV}_{0.4}\text{Mn}_{0.5}\text{Co}_{0.05}\text{Ni}_{1.1}$	AM	Co improves HRD, cycle stability, and self-discharge	[48]	2001
$\text{ZrTi}_{0.1}\text{V}_{0.2}\text{Cr}_{0.1}\text{Mn}_{0.6}\text{Co}_{0.1}\text{Ni}_{1.2}$	AM + Ann	$C_{100}$ of $390 \text{ mAh}\cdot\text{g}^{-1}$	[49]	2001
$\text{Zr}_{0.9}\text{Ti}_{0.1}\text{V}_{0.2}\text{Mn}_{0.56}\text{Co}_{0.1}\text{Ni}_{1.14}$	IM	$C_{60}$ of $350 \text{ mAh}\cdot\text{g}^{-1}$	[50]	2002
$\text{Zr}(\text{NiVMnCoSn}_x)_{2+\alpha}$	IM	Sn has detrimental effects to EC performance.	[51]	2006

**Table 3.** Summary of previous comparative studies on the hydrogen storage properties of C14 and C15 in gaseous phase (GP) or electrochemical (EC) environment.  $\Delta H_h$  denotes heat of hydride formation.

Basic Composition	Preparation Method	Application	Major Findings	References
(TiZr)V <sub>0.5</sub> Mn <sub>0.2</sub> Fe <sub>0.2</sub> Ni <sub>1.1</sub>	AM	EC	C14 has a better HRD	[52]
Zr(CrNi) <sub>2</sub>	AM + Ann	GP	No difference if composition is the same	[53]
(ZrTi)(VMnNi) <sub>x</sub>	AM	EC	C14 has a higher discharge capacity ( $x < 2$ ) C15 has a better HRD ( $x > 2$ )	[35,54]
(ZrTi)(NiMnM) <sub>x</sub> , where M = Cr, V, Co, Al	IM + Ann	EC	C15 has a better cycle life but slower activation	[40]
(ZrTi)(VMnCoNi) <sub>2</sub>	LM	EC	C14 has a higher capacity and HRD	[55]
(ZrTi)(VMnNi) <sub>2</sub>	AM	EC	With no Ti, C15 has more desirable capacities, with Ti, C14 has a high capacity	[44]
Zr(VMnNi) <sub>2</sub>	AM	EC	C15 is better with regards to capacity, HRD, and activation	[56]
(ZrTi)(VCrMnNi) <sub>2</sub>	AM	EC	C14 has a higher capacity and HRD	[57]
(ZrTi)(VMnNi) <sub>x</sub>	IM + Ann	GP	C15 has a longer cycle life	[58]
Zr(VFe) <sub>x</sub>	AM	GP	C14 has a higher H-storage capacity	[59]
(ZrTi)(VAL) <sub>2</sub>	AM	GP	C14 has a lower $\Delta H_h$	[60]
(ZrTi)(VCrMnCoNiAl) <sub>2</sub>	IM	EC	C15 has a better HRD and low-temperature performance, but shorter cycle life	[61]
(ZrTi)(VCrMnNil) <sub>2</sub>	IM	EC	C14 has a better charge retention and cycle life, but lower capacity and HRD	[62]
(ZrTi)(VCrMnCoNiAl) <sub>2</sub>	IM	EC	C15 phase improves both activation and HRD	[63]

## 2. Experimental Setup

Each ingot sample was prepared by an induction melting process under a 0.08 MPa Ar protection atmosphere and elemental raw materials with a purity of >99.9% (except for Zr, where Sn-containing (1%) zircaloy was used). An MgO crucible, an alumina tundish, and a steel mold were used for melting. Annealing was performed in vacuum (achieved with a diffusion pump) for 6 h at 960 °C with a 3 h temperature ramp-up period. The ingot was then cooled naturally to room temperature. For powder fabrication, the ingot underwent a hydriding/dehydriding process, which introduced initial volume expansion/contraction to create internal stress before it was crushed and ground to a –200 mesh powder. A Varian *Liberty* 100 inductively coupled plasma optical emission spectrometer (ICP-OES, Agilent Technologies, Santa Clara, CA, USA) was employed to study the chemical composition. A Philips X'Pert Pro XRD (X-ray diffractometer, Philips, Amsterdam, The Netherlands) was used to perform the phase analysis, and a JEOL-JSM6320F scanning electron microscope (SEM, JEOL, Tokyo, Japan) with energy dispersive spectroscopy (EDS) was also used to investigate the phase distribution and composition. A Suzuki Shokan multi-channel pressure-concentration-temperature system (PCT, Suzuki Shokan, Tokyo, Japan) was used to measure the gaseous phase H-storage characteristics. PCT measurements at 30, 60, and 90 °C were performed after activation, which consisted of a 2 h thermal cycle between room temperature and 300 °C under 2.5 MPa H<sub>2</sub> pressure. MH alloy electrodes were prepared by directly pressing the MH alloy powder onto an expanded Ni substrate (1 cm × 1 cm) with a 10-ton press without the use of any metallic or organic binder. Electrochemical measurements, including capacities at various rates, bulk diffusion coefficient ( $D$ ), and surface exchange current ( $I_o$ ) were performed on an Arbin Instruments BT-2143 Battery Test Equipment (Arbin Instruments, College Station, TX, USA). A Solartron 1250 Frequency Response Analyzer (Solartron Analytical, Leicester, UK) with a sine wave amplitude of 10 mV and a frequency range of 0.5 mHz to 10 kHz was used to conduct the alternating current (AC) impedance measurements. A Digital Measurement Systems Model 880 vibrating sample magnetometer (MicroSense, Lowell, MA, USA) was used to measure the magnetic susceptibility of the activated alloy surfaces (etched for 4 h in 30 wt % KOH at 100 °C).

## 3. Results and Discussion

Two compositions, Zr<sub>21.5</sub>Ti<sub>12.0</sub>V<sub>10.0</sub>Cr<sub>7.5</sub>Mn<sub>8.1</sub>Co<sub>8.0</sub>Ni<sub>32.2</sub>Sn<sub>0.3</sub>Al<sub>0.4</sub> and Zr<sub>25.0</sub>Ti<sub>6.5</sub>V<sub>3.9</sub>Mn<sub>22.2</sub>Fe<sub>3.8</sub>Ni<sub>38.0</sub>La<sub>0.3</sub>, were selected for this comparative study. Their target compositions and ICP results are summarized in

**Table 4.** The first composition is a stoichiometric C14 composition and was used as the base alloy for a number of comparative studies [8,63–66] due to its overall balanced performance with regard to activation, HRD, and cycle stability. The  $e/a$  of the first composition is below the C14/C15 threshold ( $e/a \sim 6.9$  [24]), and therefore a C14-predominated structure occurs. The second composition was chosen based on a series of refinements targeting high-rate Ni/MH applications, and further by containing an optimized Ti and Zr ratio with Ni, Mn, V, and Fe, with a minor amount of La additive [67]. The half-cell capacity for the alloy with the second composition mixed with 80% carbonyl nickel approached  $460 \text{ mAh}\cdot\text{g}^{-1}$  at a discharge current density of  $10 \text{ mA}\cdot\text{g}^{-1}$  [68]. Compared to the first composition, the second composition is hyperstoichiometric and has a higher Zr-content, lower V-content, no Cr, and higher Ni-content, which contribute to a higher  $e/a$  value and result in a C15-predominated alloy. A small amount of La was added in the C15-predominated alloy to facilitate the activation process [37,69,70]. While only the un-annealed C14 alloy was used for this comparative work, two versions of the C15 alloys were assessed: pristine (C15) and annealed alloys (C15A). Since the effects of annealing on the multi-phase C14-predominated  $\text{AB}_2$  MH alloys have been well studied (elimination/reduction in secondary phase abundance results in reduction of synergetic effects, leading to deterioration of electrochemical properties) [55,61,71,72], only the impacts of annealing on the C15  $\text{AB}_2$  MH alloy will be verified in this work. ICP results of the three alloys (C14, C15, and C15A) are in excellent agreement with the corresponding design values.

**Table 4.** Design compositions (in **bold**) and ICP results in at %.  $e/a$  is the average electron density. B/A is the atomic ratio of B-atom (elements other than Ti and Zr, and La) to A-atom (Ti, Zr, and La).

Alloy	Source	Zr	Ti	V	Cr	Mn	Fe	Co	Ni	Sn	Al	La	$e/a$	B/A
C14	Design	<b>21.5</b>	<b>12.0</b>	<b>10.0</b>	<b>7.5</b>	<b>8.1</b>	-	<b>8.0</b>	<b>32.2</b>	<b>0.3</b>	<b>0.4</b>	-	<b>6.82</b>	<b>1.99</b>
	ICP	21.5	12.0	10.0	7.5	8.1	-	8.0	32.2	0.4	0.3	-	6.82	1.99
C15	Design	<b>25.0</b>	<b>6.5</b>	<b>3.9</b>	-	<b>22.2</b>	<b>3.8</b>	-	<b>38.0</b>	<b>0.3</b>	<b>0.0</b>	<b>0.3</b>	<b>7.13</b>	<b>2.14</b>
	ICP	24.7	6.5	3.9	-	21.9	4.2	-	38.3	0.3	0.1	0.2	7.16	2.18
C15A	Design	<b>25.0</b>	<b>6.5</b>	<b>3.9</b>	-	<b>22.2</b>	<b>3.8</b>	-	<b>38.0</b>	<b>0.3</b>	<b>0.0</b>	<b>0.3</b>	<b>7.13</b>	<b>2.14</b>
	ICP	24.9	6.5	3.9	-	21.8	4.2	-	38.2	0.3	0.1	0.2	7.15	2.16

### 3.1. X-Ray Diffractometer Analysis

XRD analysis was used to study the constituent phases occurring in the alloys. The obtained XRD patterns are shown in Figure 3. The XRD pattern from the C14 alloy demonstrates a C14-predominated structure with overlapping C15 peaks and a minor TiNi peak. Both XRD patterns from C15 and C15A alloys show a C15 structure with a small ZrNi peak in the pristine alloy. Results from full XRD pattern fitting with Jade 9.0 software (MDI, Livermore, CA, USA) are summarized in Table 5. The  $c/a$  ratio obtained for the C14 alloy (1.629) is only slightly lower than the ideal ratio (1.633), and this deviation is commonly seen in C14 alloys for Ni/MH application. The atomic size ratio,  $R_A/R_B$  (where  $R_A$  and  $R_B$  represent the average atomic radii of the A-site and B-site atoms, respectively), in the C14 alloy (1.216) is slightly lower than the ideal ratio of  $\sqrt{\frac{3}{2}} \cong 1.225$  [73], which causes a deviation in the  $c/a$  ratio from the ideal value. Moreover, the secondary phases found in the C14 and C15 alloys belong to TiNi and ZrNi structures, respectively. After annealing, the ZrNi secondary phase in the C15 alloy becomes undetectable. This reduction/diminishing of the secondary phase after annealing also occurs in the C14  $\text{AB}_2$  MH alloys [55,61,71,72]. In addition to C14 and TiNi, there is also a 5.2 wt % of C15 found in the C14 alloy since the alloy's  $e/a$  (6.82) is close to the  $e/a$  at the C14/C15 threshold for Zr/Ti ( $\cong 1.8$  (6.91)) [24]. The C15 phase is usually located between the C14 main matrix and other  $\text{Zr}_x\text{Ni}_y$  secondary phases [74]. Therefore, due to the mixed nature of the C14 and C15 phases in the C14 alloy, the crystallites in the C14 alloy are smaller than those in the C15 alloy. Furthermore, the annealed C15 (C15A) has even larger crystallites. The increase in crystallite size after annealing is a common observation in Laves phase-based MH alloys [61,75].

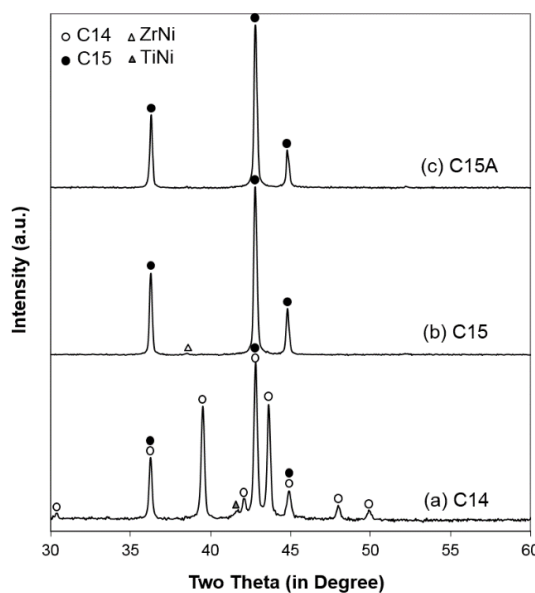


**Figure 3.** X-ray diffractometer patterns using Cu-K $\alpha$  as the radiation source for the various alloys. (a) C14, (b) C15, and (c) C15A.

**Table 5.** Lattice constants, abundance, crystallite size (CS) of the C14 and C15 phases of the C14, C15, and C15A alloys. Abundances of TiNi and ZrNi secondary phases are also included.

Alloy	C14	C15	C15A
C14 Lattice constant $a$ , nm	0.49545	-	-
C14 Lattice constant $c$ , nm	0.80733	-	-
C14 Abundance, wt%	93.7	-	-
C14 CS, nm	68	-	-
C15 Lattice constant $a$ , nm	0.69932	0.70061	0.70047
C15 Abundance, %	5.2	99.3	100
C15 CS, nm	54	96	>100
TiNi Abundance, wt%	1.2	-	-
ZrNi Abundance, wt%	-	0.7	-

### 3.2. Scanning Electron Microscope/Energy Dispersive Spectroscopy Analysis

SEM back-scattering electron images (BEI) from the alloys are presented in Figure 4. The composition of several representative areas (identified by Roman numerals) in the SEM micrographs were studied by EDS, and the results are summarized in Table 6. SEM micrographs of the C14 alloy shows a very typical multi-phase C14-C15-Zr<sub>x</sub>Ni<sub>y</sub> microstructure, which has been extensively studied with transmission electron microscopy (TEM) [76,77] and electron backscattering diffraction (EBSD) [75]. Occasional ZrO<sub>2</sub> inclusions are also seen in the C14 alloy and act as oxygen scavengers [78], which may contribute positively to the bulk diffusion of hydrogen and provide surface protection against oxidation by the electrolyte [79]. In the SEM micrographs of the C15 and C15A alloys, a LaNi or La-rich phase with a high contrast is observed, suggesting segregation of La from the main phase. Since La does not precipitate into the Zr-based Laves phase, it segregates into a LaNi secondary phase, as in the cases of other rare earth element substitutions [9]. The relatively high solubility of the LaNi phase in the KOH electrolyte results in the facilitation of an initial formation process in alkaline solution [70]. The La-content and Ni-content of the La-rich secondary phase in the C15 alloy increases and decreases after annealing, respectively. It should be noted that the XRD analysis does not detect any La-containing phase, due to its small overall abundance. In addition, the SEM micrographs shown in Figure 4 are not typical, but exhibit the most features and therefore reveal all phases of the alloys. Additionally, the measured Sn-content in the LaNi phase before annealing is quite high (15.7 at %) and becomes even higher (21.5 at %) after annealing.

In the Laves phase MH alloys, Sn dissolves into the main C14 Laves phase and the ZrNi secondary phase without forming any Sn-rich secondary phase [8,78,80–84], and more Sn migrates into the ZrNi secondary phase after annealing [61]. The presence of Sn in the composition of the Zr-containing MH alloy is due to a cost saving consideration—the market price of Sn-containing zircaloy scrap, which is used as one of the raw materials in the current study, at one time was only one tenth of the cost of pure Zr scrap. In general, a small percentage of Sn (approximately 0.2 to 0.4 at %), if dissolved fully into the main phase, facilitates hydride formation but reduces HRD and cycle life [79]. Moreover, a phase with a slightly brighter contrast (Spot 2 in Figure 4b) and a composition close to (Zr,Ti)Ni can be found in the C15 alloy. It is eliminated during the annealing process and disappears in the SEM micrograph taken from the C15A alloy (Figure 4c).

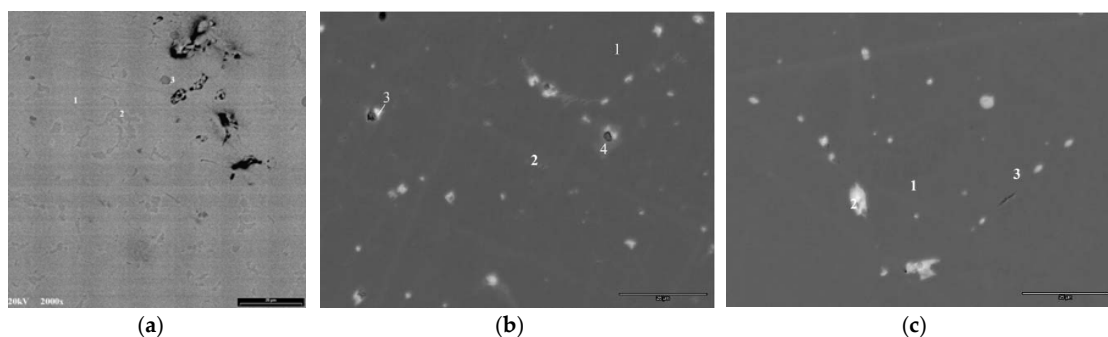


**Figure 4.** SEM BEI micrographs from the (a) C14, (b) C15, and (c) C15A alloys. The composition of the numbered areas was analyzed by EDS and the results are shown in Table 6. The bar at the lower right corner in each micrograph represents 25  $\mu\text{m}$ .

**Table 6.** Summary of the EDS results. All compositions are in %. Compositions of the main AB<sub>2</sub> phase are in **bold**.

Location	Zr	Ti	V	Cr	Mn	Fe	Co	Ni	La	Sn	B/A	e/a	Phase
<b>C14-1</b>	<b>19.4</b>	<b>14.6</b>	<b>8.6</b>	<b>5.1</b>	<b>7.5</b>	<b>0.0</b>	<b>6.4</b>	<b>38.3</b>	<b>0.0</b>	<b>0.1</b>	<b>1.94</b>	<b>6.46</b>	<b>AB<sub>2</sub></b>
C14-2	18.0	23.3	3.0	1.4	3.5	0.0	5.1	45.6	0.0	0.1	1.42	-	TiNi
C14-3	80.4	3.9	3.4	2.2	2.1	0.0	1.3	6.2	0.0	0.5	0.19	-	ZrO <sub>2</sub>
<b>C15-1</b>	<b>24.6</b>	<b>6.5</b>	<b>3.7</b>	<b>0.0</b>	<b>22.2</b>	<b>4.4</b>	<b>0.0</b>	<b>38.6</b>	<b>0.0</b>	<b>0.0</b>	<b>2.22</b>	<b>7.20</b>	<b>AB<sub>2</sub></b>
C15-2	23.6	15.2	0.9	0.0	8.4	1.4	0.0	50.2	0.3	0.0	1.56	-	ZrNi
C15-3	5.0	1.7	0.7	0.0	4.7	0.8	0.0	20.9	50.5	15.7	0.75	-	LaNi
C15-4	15.6	5.3	1.3	0.0	7.5	1.2	0.0	26.4	40.9	1.8	0.62	-	Oxide
<b>C15A-1</b>	<b>24.8</b>	<b>6.5</b>	<b>3.8</b>	<b>0.0</b>	<b>22.6</b>	<b>4.2</b>	<b>0.0</b>	<b>37.9</b>	<b>0.1</b>	<b>0.0</b>	<b>2.18</b>	<b>7.15</b>	<b>AB<sub>2</sub></b>
C15A-2	0.6	0.2	0.5	0.0	0.7	0.1	0.0	11.1	61.3	25.5	0.61	-	La-rich
C15A-3	58.7	5.6	2.1	0.0	12.2	2.4	0.0	19.0	0.0	0.0	0.56	-	ZrO <sub>2</sub>

### 3.3. Pressure-Concentration-Temperature Analysis

The PCT isotherms were measured at 30, 60, and 90 °C, and the results from the first two temperatures are shown in Figure 5. PCT isotherms measured at 90 °C are not complete due to an increase in plateau pressure (out of range for the testing apparatus), and therefore are not shown. Gaseous phase H-storage characteristics obtained from the PCT analysis are summarized in Table 7. Compared to the C14 alloy, the PCT isotherms of both the C15 and C15A alloys show a very steep takeoff from the  $\alpha$  (metal)-to- $\beta$  (metal hydride) region, which is similar to the observations seen in Nd-based AB<sub>5</sub> [85] and A<sub>2</sub>B<sub>7</sub> [86] MH alloys, and a lower self-discharge is expected. Moreover, the C15 and C15A alloys show very flat plateaus, which are extremely uncommon in multi-phase MH alloys [8,87]. In order to quantify the plateau flatness, slope factor (as previously defined in [8]: the ratio of storage capacity between 0.01 MPa and 0.5 MPa to total capacity in the desorption isotherm) of each alloy was calculated. The increase in slope factor (plateau flatness) from the C14 alloy (0.60) to the C15 and C15A alloys (0.87 and 0.90, respectively) is a direct result of the elimination of multi-phase

features and the accompanying synergistic mode [88]. Annealing of the C15 alloy decreases the storage capacity, slightly decreases the plateau pressure, and increases the absorption/desorption hysteresis (defined as  $\ln\left(\frac{\text{absorption plateau pressure}}{\text{desorption plateau pressure}}\right)$ ) in the middle of the pressure plateau due to the improvement in the homogeneity and complete removal of the ZrNi secondary phase, which is very critical for supplying the synergistic effects [89,90]. Several speculations have been proposed for the possible origin of PCT hysteresis [91–94]. The energy required for elastic lattice deformation in the metal/MH interface area during absorption [95] is currently the most accepted explanation. The reduction in PCT hysteresis in the multi-phase system has been explained previously and is caused by the remaining hydrogenated phase (from activation or previous hydrogenation) at the grain boundary between phases (Figure 14 in [89]). Cleanliness at the interface (free of amorphous and impurity phase) between phases removes a possible source for dissipation of stresses at a boundary between the major and the secondary phases and is important for the occurrence of such phenomenon. It has been confirmed in similar alloys through the use of TEM and EBSD [74,96]. Therefore, the C14 alloy, that has the highest secondary phase abundance (6.4 wt %), also has the smallest PCT hysteresis (0.04); the C15 alloy, that has a lower secondary phase abundance (0.7 wt %), has a larger PCT hysteresis (0.13), while the C15A alloy has no detectable (through XRD analysis) secondary phase and shows the largest PCT hysteresis (0.31). Synergistic effects resulted by the presence of the secondary phase and composition inhomogeneity reduce the hysteresis and make more storage sites accessible, so the plateau region of the PCT isotherm can be extended [89]. Furthermore, both the  $\Delta H_h$  and difference in entropy ( $\Delta S_h$ ) were estimated using desorption plateau pressures at 30 and 60 °C with the following equation:

$$\Delta H_h - T \Delta S_h = \mathfrak{R} T \ln P \quad (1)$$

where  $\mathfrak{R}$  is the ideal gas constant and  $T$  is the absolute temperature. Although the C15 alloy has a significantly higher plateau pressures compared to the C14 alloy, they exhibit similar  $\Delta H_h$  values, which indicates that the current comparative study between C14 and C15 is fair. After annealing, the C15A alloy demonstrates a lower  $\Delta H_h$  (more stable hydride) and a  $\Delta S_h$  closer to the ideal value between free hydrogen gas and solid ( $-130.7 \text{ J}\cdot\text{mol}^{-1}\cdot\text{K}^{-1}$ ) [97]. The formation of the more ordered hydride from C15A is resulted by the improvement in homogeneity by annealing.

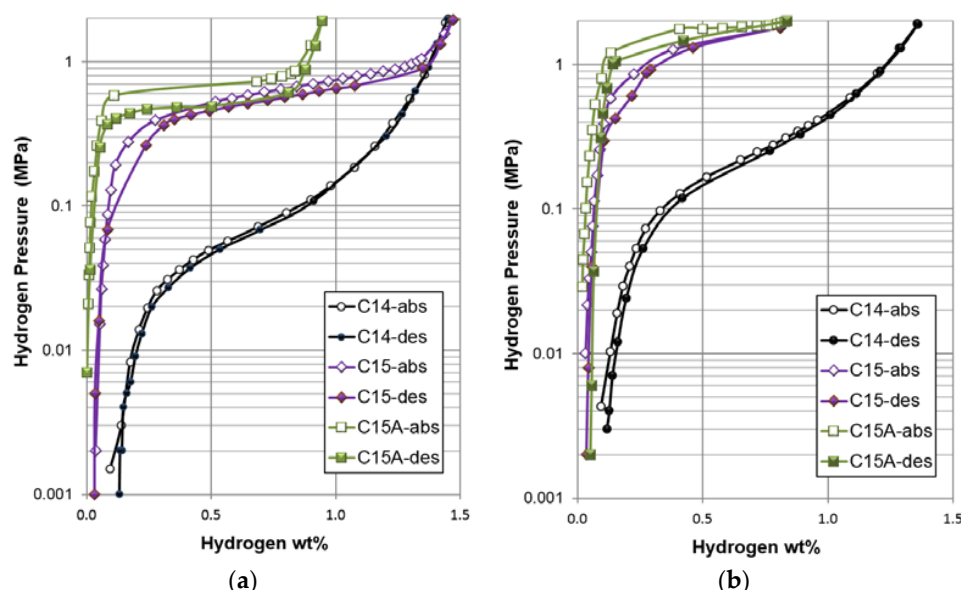


**Figure 5.** Pressure-concentration-temperature (PCT) isotherms from the C14, C15, and C15a alloys measured at (a) 30 and (b) 60 °C. Open and solid symbols represent the absorption and desorption curves, respectively.

**Table 7.** Summary of the gaseous phase properties of the C14, C15, and C15A AB<sub>2</sub> alloys.

Alloy	C14	C15	C15A
Maximum Capacity @ 30 °C in wt%	1.45	1.47	0.95
Reversible Capacity @ 30 °C in wt%	1.32	1.44	0.94
Desorption Pressure @ 30 °C in MPa	0.078	0.55	0.50
Slope Factor @ 30 °C	0.60	0.87	0.90
PCT Hysteresis @ 30 °C	0.04	0.13	0.31
−ΔH <sub>h</sub> in kJ·mol <sup>−1</sup>	32	31.8	35.4
−ΔS <sub>h</sub> in J·mol <sup>−1</sup> ·K <sup>−1</sup>	104	119	130

### 3.4. Electrochemical Analysis

The electrochemical capacity and activation characteristics of the alloys were studied using half-cell measurements in a flooded configuration (for details, see [98]). Evolution of full capacity (measured at a discharge rate of 4 mA·g<sup>−1</sup>) and HRD (the ratio of capacity at a discharge rate of 50 mA·g<sup>−1</sup> to that at a discharge rate of 4 mA·g<sup>−1</sup>) for the first 13 cycles are plotted in Figure 6, and the electrochemical properties are summarized in Table 8. Figure 6 shows that the C14 alloy has a higher low-rate capacity, a lower HRD, and is more difficult to activate, compared to the C15 alloys. Since the C15 and C15A alloys' plateaus pressures are higher than 0.1 MPa (one atmosphere) and therefore cannot be fully charged in the open-to-air half-cell configuration, their discharge capacities are lower than the expected values from the conversion of the gaseous phase H-storage capacities (1 wt % = 268 mAh·g<sup>−1</sup>). If the C15 alloy powder samples are entirely embedded in a soft metallic binder (Ni or Cu), their full capacities can be obtained [68]. However, for our measurements, the MH powder was directly compacted onto a Ni substrate without any binder or metallic fine particles, which results in the easy release of hydrogen gas from the surface and incomplete charge. Moreover, the C15 and C15A alloys show better HRD and activation performances than the C14 alloy, and the HRD of the C15 alloy is slightly higher than that of the C15A alloy, due to the eliminations of the secondary phase and accompanied synergic effect by annealing. We believe that the differences in activation, degradation, and HRD originated from the composition rather than the structure. By comparing the compositions of alloys C14 and C15 (Table 4), Cr, a very important substitution element in the MH alloy for the enhancement of corrosion resistance by forming the V-Cr-based solid solution secondary phase [78,99], is absent in alloy C15. Alloy C15 also has a higher Ni-content, which is known for achieving a better HRD performance [100,101]. While the Cr-containing alloy C14 is more difficult to activate but maintains the discharge capacity in the first 13 cycles, the Cr-free alloy C15 shows some capacity degradation. After annealing, the capacity degradation of alloy C15A is improved but still noticeable in cycles 9 to 13 (Figure 6a).

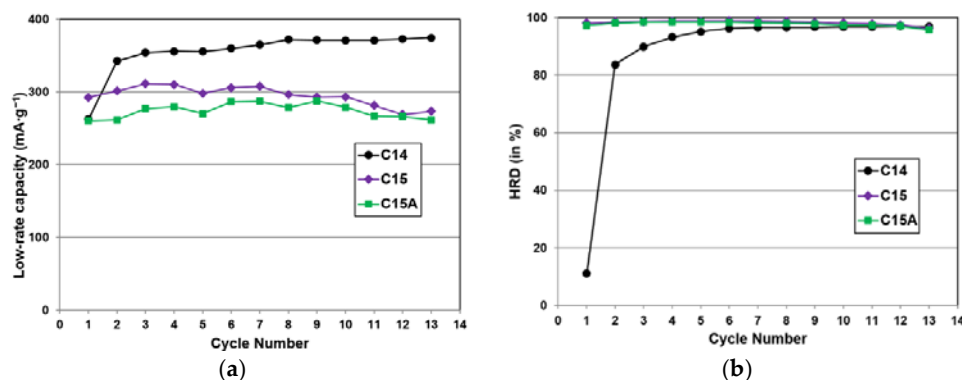


**Figure 6.** Activation behaviors observed from (a) full capacity (measured at low-rate) and (b) HRD for the first 13 electrochemical cycles measured at room temperature.

**Table 8.** Summary of the room temperature electrochemical and magnetic results (capacity, rate,  $D$ ,  $I_o$ , and  $M_S$ ,  $H_{1/2}$ ) of C14, C15, and C15A alloys. RT denotes room temperature.

Alloy	C14	C15	C15A
3 <sup>rd</sup> cycle capacity @50 mA·g <sup>-1</sup> in mAh·g <sup>-1</sup>	318	307	273
3 <sup>rd</sup> cycle capacity @4 mA·g <sup>-1</sup> in mAh·g <sup>-1</sup>	354	311	277
HRD @ 3 <sup>rd</sup> cycle	0.9	0.99	0.98
Activation cycle to reach 95% HRD	5	1	1
Diffusion coefficient, $D$ @ RT in 10 <sup>-10</sup> cm <sup>2</sup> ·s <sup>-1</sup>	2.5	2.4	1.6
Exchange current, $I_o$ @ RT in mA·g <sup>-1</sup>	22.5	46.8	39.4
$M_S$ in emu·g <sup>-1</sup>	0.037	0.042	0.017
$H_{1/2}$ in kO <sub>2</sub>	0.11	0.26	0.48

The superiority in HRD of alloys C15 and C15A was further investigated by electrochemically measuring  $D$  and  $I_o$ .  $D$  was measured by a potentiostatic discharge process—the electrode was first fully charged and then discharged at a potential of +0.6 V for 7200 s, and the anodic current response is tracked with respect to time during the process. Figure 7a shows the resulted semi-logarithmic curves of the anodic current response vs. time for the three alloys.  $D$  was estimated using the slope of the linear region of the semi-logarithmic response according to the equation [102]:

$$\log i = \log\left(\frac{6FD}{da^2}(C_0 - C_s)\right) - \frac{\pi^2}{2.303} \frac{D}{a^2} t \quad (2)$$

where  $i$  is the specific diffusion current (A·g<sup>-1</sup>),  $F$  is the Faraday constant,  $C_0$  is the initial hydrogen concentration in the alloy bulk (mol·cm<sup>-3</sup>),  $C_s$  is the hydrogen concentration on the surface of the alloy particles (mol·cm<sup>-3</sup>),  $d$  is the density of the H-storage alloy (g·cm<sup>-3</sup>),  $a$  is the alloy particle radius (cm), and  $t$  is the discharge time (s).  $I_o$  was measured by linear polarization, specifically the electrode was first fully charged, then discharged to 50% depth-of-discharge, and then scanned within a small overpotential range of ±10 mV. In this small overpotential range, the current vs. overpotential shows a linear dependence, as seen in Figure 7b, and  $I_o$  can be obtained from the equation [103]:

$$I_o = \frac{iRT}{F\eta} \quad (3)$$

where  $i$  is the specific current (A·g<sup>-1</sup>),  $F$  is the Faraday constant, and  $\eta$  is the overpotential. Further details for the  $D$  and  $I_o$  calculations have been previously reported [98], and the  $D$  and  $I_o$  values for the current set of alloys are listed in Table 8. While the  $D$  values of the C14 and C15 alloys are close, it deteriorates after annealing for the C15 alloy, due to the elimination of the secondary phase. The main difference between the C14 and C15 alloys occurs in the surface reaction, where  $I_o$  in the C15 alloy is more than double that of the C14 alloy. The  $I_o$  value found for the C15 alloy is even higher than that in an AB<sub>5</sub> MH alloy that has a higher Ni-content [104]. After annealing,  $I_o$  decreases, which confirms the positive contribution of the ZrNi secondary phase to the surface reaction. ZrNi is more susceptible to dissolution in KOH solution, and its existence in the AB<sub>2</sub> MH alloys has been shown to improve HRD [62]. In conclusion, the superior HRD of the C15 alloy comes from the higher  $I_o$  value, which indicates a faster surface reaction.

In order to investigate the source of the faster surface reaction (higher  $I_o$ ) found in the C15 alloy, AC impedance measurements were conducted at both room temperature (RT) and −40 °C. The charge-transfer resistance ( $R$ ) and double-layer capacitance ( $C$ ) obtained from Cole-Cole plots [88] are listed in Table 9. There are two factors dominating the  $R$  values: the amount of reactive surface area and surface reaction catalytic ability. While the former is directly proportional to the capacitance, the latter can be related to the  $RC$  product (a higher  $RC$  corresponds to a worse catalytic surface) [105]. From the comparisons in Table 9, the C15 alloy has lower  $R$  values at both RT and −40 °C, mainly

due to its higher amount of reactive surface area (higher C), which is closely related to the addition of La [70]. In addition, the surface catalytic abilities of the C15 alloy at RT and  $-40^{\circ}\text{C}$  are the same as and slightly worse, respectively, than those of the C14 alloy. Therefore, we conclude that the higher  $I_0$  of the C15 alloy originates from the higher amount of reactive surface, which is due to the additional La, an absence of Cr, and a higher Mn-content in the composition. As for the annealing effects for the C15 alloy, the data in Table 9 show deteriorated R's at both RT and  $-40^{\circ}\text{C}$  after annealing, which is due to the reduction in reactive surface area. The unchanged RC product with annealing requires further investigation and is discussed in the next section.

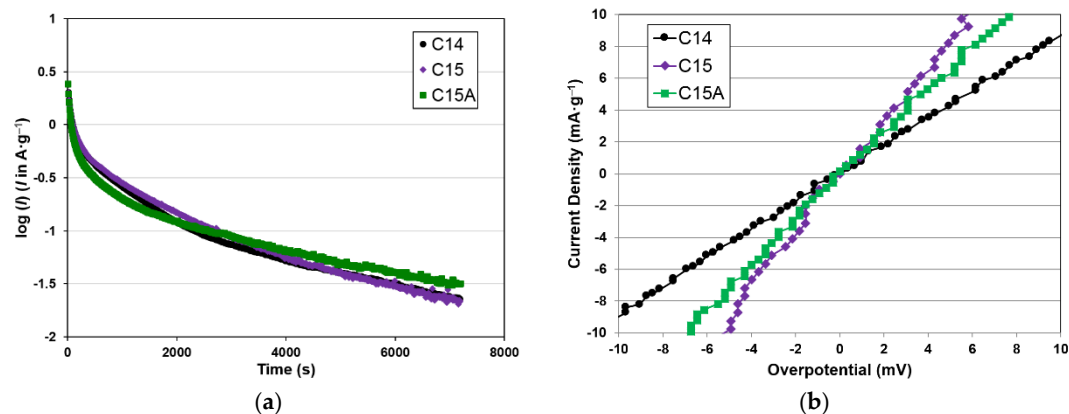


**Figure 7.** (a) Semilogarithmic curves of anodic current vs. time during potentiostatic discharge and (b) linear polarization curves measured at 50% depth-of-discharge from the C14, C15, and C15A alloys.

**Table 9.** A summary of the electrochemical results from AC impedance measurement ( $R$ —charge transfer resistance,  $C$ —double-layer capacitance) at room temperature (RT) and  $-40^{\circ}\text{C}$  for the C14, C15, and C15A alloys.

Property	$R @ \text{RT}$	$C @ \text{RT}$	$RC$	$R @ -40^{\circ}\text{C}$	$C @ -40^{\circ}\text{C}$	$RC$
Unit	$\Omega \cdot \text{g}$	$\text{Farad} \cdot \text{g}^{-1}$	s	$\Omega \cdot \text{g}$	$\text{Farad} \cdot \text{g}^{-1}$	s
C14	0.32	0.34	0.11	29	0.24	7.0
C15	0.23	0.49	0.11	22	0.49	10.7
C15A	0.32	0.34	0.11	26	0.41	10.7

### 3.5. Magnetic Susceptibility Analysis

Measuring saturated values of magnetic susceptibility ( $M_s$ ) is a convenient way to quantify the amount of catalytic metallic Ni clusters embedded in the surface oxide, which has been shown to strongly influence the surface catalytic ability of MH alloys for electrochemical reactions [79,104,106]. However, recent TEM studies revealed that other fine surface structures in the Si- [82] and La- [70] containing AB<sub>2</sub> MH alloys can also affect surface catalytic ability. Furthermore, applied magnetic fields corresponding to half of  $M_s$  ( $H_{1/2}$ ) can be used as a parameter to quantify the size of the metallic clusters; more specifically, it is inversely proportional to the size of the magnetic domain of these clusters [8]. Results of  $M_s$  and  $H_{1/2}$  from the three alloys in this study are listed in the last two columns in Table 8. The C15 alloy has a slightly higher  $M_s$  (more catalytic surface) and  $H_{1/2}$  (smaller metallic clusters) compared to the C14 alloy, which may be related to the larger surface area of the C15 alloy (higher RT C in Table 9). After annealing,  $M_s$  is reduced by a large amount, but this change in  $M_s$  is not reflected in the  $RC$  product. Other factors, such as the change in composition of the La-containing phase (increases in La and Sn but reduction in Ni) after annealing, may be the cause of the unchanged catalytic ability, even though  $M_s$  is reduced with annealing.

#### 4. Conclusions

The gaseous phase and electrochemical hydrogen storage characteristics of two Laves phase MH alloys are compared. In order to secure the dominance of a single phase, a composition with a higher percentage of transition metals with lower number of valence electrons (V and Cr) was adopted to achieve a low average electron density and the consequent C14-predominated alloy (Alloy C14), and a composition designed oppositely is also adopted to acquire a C15-predominated alloy (Alloy C15). The following performance variations are most likely linked to composition differences, rather than structural difference. Alloy C15 in this study has a higher plateau pressure, lower gaseous phase storage capacities under 2 MPa (both maximum and reversible), and a lower discharge capacity compared to Alloy C14. The flatter PCT isotherm with a larger hysteresis and a smaller change in entropy in Alloy C15 are due to the higher uniformity in the alloy (higher main phase abundance). The increased high-rate performance of Alloy C15 originates from its larger surface exchange current, which is the result of a higher amount of surface area from the addition of La. The effects of annealing on Alloy C15 are identified as similar to those on the C14-predominated MH alloys, specifically elimination/reduction in secondary phase abundance, which causes deterioration in the gaseous phase and electrochemical hydrogen storage performances. However, the surface catalytic ability is unchanged after annealing, even though a reduction in the total volume of surface metallic Ni inclusions is observed. Therefore, other causes, such as a change in composition of the La-rich secondary phase after annealing, may be in play. In summary, from the two compositions used in this study, Alloy C15 is recommended for applications requiring high capacity and long cycle durability, while Alloy C15 is more geared toward those requiring high-rate capability and easy formation.

**Acknowledgments:** The authors would like to thank the following individuals from BASF-Ovonic for their assistance: Taihei Ouchi, Su Cronogue, Baoquan Huang, Diana F. Wong, David Pawlik, Allen Chan, and Ryan J. Blankenship. The work is related to the collaboration between IFE and BASF on the project MoZEEs, funded by Norwegian Research Council.

**Author Contributions:** Kwo-Hsiung Young designed the experiments. Jean Nei performed the experiments. Chubin Wan, Roman V. Denys and Volodymyr A. Yartys analyzed the results and prepared the manuscript.

**Conflicts of Interest:** The authors declare no conflict of interest.

#### Abbreviations

Ni/MH	Nickel/metal hydride
MH	Metal hydride
fcc	Face-centered cubic
H-site	Hydrogen occupying site
H-storage	Hydrogen storage
e/a	Average electron density
HRD	High-rate dischargeability
AM	Arc melting
Ann	Annealing
PM	Plasma melting
LM	Levitation melting
IM	Induction melting
C <sub>m</sub>	Discharge capacity obtained at an <i>m</i> mA·g <sup>-1</sup> discharge current
GP	Gaseous phase
EC	Electrochemical
ΔH <sub>h</sub>	Heat of hydride formation
ICP-OES	Inductively coupled plasma optical emission spectrometer
XRD	X-ray diffractometer
SEM	Scanning electron microscope
EDS	Energy dispersive spectroscopy
PCT	Pressure concentration temperature

D	Bulk diffusion coefficient
$I_0$	Surface exchange current
AC	Alternating current
$R_A$	Average atomic radius of the A-site atoms
$R_B$	Average atomic radius of the B-site atoms
CS	Crystallite size
BEI	Back-scattering electron image
TEM	Transmission electron microscope
EBSD	Electron backscattering diffraction
$\alpha$	Metal
$\beta$	Metal hydride
$\Delta S_h$	Change in entropy
R	Ideal gas constant
T	Absolute temperature
i	Specific diffusion current
F	Faraday constant
$C_o$	Initial hydrogen concentration in alloy bulk
$C_s$	Hydrogen concentration on alloy particle surface
d	Density of hydrogen storage alloy
a	Alloy particle radius
t	Discharge time
$\eta$	Overpotential
RT	Room temperature
R	Surface charge-transfer resistance
C	Surface double-layer capacitance
$M_s$	Saturated magnetic susceptibility
$H_{1/2}$	Applied magnetic field strength corresponding to half of saturated magnetic susceptibility

## References

- Young, K.; Ng, K.Y.S.; Bendersky, L.A. A technical report of the Robust Affordable Next Generation Energy Storage System-BASF Program. *Batteries* **2016**, *2*. [[CrossRef](#)]
- Young, K.; Ouchi, T.; Koch, J.; Fetcenko, M.A. The role of Mn in C14 Laves phase multi-component alloys for NiMH battery application. *J. Alloys Compd.* **2009**, *477*, 749–758. [[CrossRef](#)]
- Chang, S.; Young, K.; Nei, J.; Fierro, C. Reviews on the U.S. Patents regarding nickel/metal hydride batteries. *Batteries* **2016**, *2*, 10. [[CrossRef](#)]
- Young, K.; Yasuoka, S. Capacity degradation mechanisms in nickel/metal hydride batteries. *Batteries* **2016**, *2*. [[CrossRef](#)]
- Yurchenko, N.; Stepanov, N.; Salishchev, G. Laves-phase formation criterion for high-entropy alloys. *Mater. Sci. Tech.* **2017**, *33*, 17–22. [[CrossRef](#)]
- Pearson, W.B. *The Crystal Chemistry and Physics of Metals and Alloys*; John Wiley & Sons: New York, NY, USA, 1972; p. 24.
- Aufrecht, J.; Leineweber, A.; Mittemeijer, E.J. Metastable hexagonal modifications of the NbCr<sub>2</sub> Laves phase as function of cooling rate. *Mater. Res. Soc. Symp. Proc.* **2009**, *1128*. [[CrossRef](#)]
- Chang, S.; Young, K.; Ouchi, T.; Meng, T.; Nei, J.; Wu, X. Studies on incorporation of Mg in Zr-based AB<sub>2</sub> metal hydride alloys. *Batteries* **2016**, *2*. [[CrossRef](#)]
- Young, K.; Ouchi, T.; Nei, J.; Moghe, D. The importance of rare-earth additions in Zr-based AB<sub>2</sub> metal hydride alloys. *Batteries* **2016**, *2*. [[CrossRef](#)]
- Ivey, D.; Northwood, D. Hydrogen site occupancy in AB<sub>2</sub> Laves phases. *J. Less-Common Met.* **1986**, *115*, 23–33. [[CrossRef](#)]
- Yartys, V.A.; Burnasheva, V.V.; Semmenenko, K.N.; Fadeeva, N.V.; Solov'ev, S.P. Crystal chemistry of RT<sub>5</sub>H(D)<sub>x</sub>, RT<sub>2</sub>H(D)<sub>x</sub> and RT<sub>3</sub>H(D)<sub>x</sub> hydrides based on intermetallic compounds of CaCu<sub>5</sub>, MgCu<sub>2</sub>, MgZn<sub>2</sub> and PuNi<sub>3</sub> structure types. *Int. J. Hydrogen Energy* **1982**, *7*, 957–965. [[CrossRef](#)]

12. Gingl, F.; Yvon, K.; Vogt, T.; Hewat, A.W. Synthesis and crystal structure of tetragonal  $\text{LnMg}_2\text{H}_7$  ( $\text{Ln}=\text{La}$ ,  $\text{Ce}$ ), two Laves phase hydride derivatives having ordered hydrogen distribution. *J. Alloys Compd.* **1997**, *253*, 313–317. [[CrossRef](#)]
13. Shoemaker, D.P.; Shoemaker, C.B. Concerning atomic sites and capacities for hydrogen absorption in the  $\text{AB}_2$  Friauf-Laves phases. *J. Less-Common Met.* **1979**, *68*, 43–58. [[CrossRef](#)]
14. Midden, H.J.P.; Prodan, A.; Zupanič, E.; Žitko, R.; Makridis, S.S.; Stubos, A.K. Structural and electronic properties of the hydrogenated  $\text{ZrCr}_2$  Laves phase. *J. Phys. Chem. C* **2010**, *114*, 4221–4227. [[CrossRef](#)]
15. Hong, S.; Fu, C.L. Hydrogen in Laves phase  $\text{ZrX}_2$  ( $X = \text{V}, \text{Cr}, \text{Mn}, \text{Fe}, \text{Co}, \text{Ni}$ ) compounds: Binding energies and electronic and magnetic structure. *Phys. Rev. B* **2002**, *66*, 094109. [[CrossRef](#)]
16. Li, F.; Zhao, J.; Tian, D.; Zhang, H.; Ke, X.; Johansson, B.J. Hydrogen storage behavior in C15 Laves phase compound  $\text{TiCr}_2$  by first principles. *J. Appl. Phys.* **2009**, *105*, 043707. [[CrossRef](#)]
17. Merlino, A.R.; Luna, C.R.; Juan, A.; Pronsato, M.E. A DFT study of hydrogen storage in  $\text{Zr}(\text{Cr}_{0.5}\text{Ni}_{0.5})_2$  Laves phase. *Int. J. Hydrogen Energy* **2016**, *41*, 2700–2710. [[CrossRef](#)]
18. Westlake, D.G. A geometric model for the stoichiometry and interstitial site occupancy in hydrides (deuterides) of  $\text{LaNi}_5$ ,  $\text{LaNi}_4\text{Al}$  and  $\text{LaNi}_4\text{Mn}$ . *J. Less-Common Met.* **1983**, *91*, 275–292. [[CrossRef](#)]
19. Stein, F.; Palm, M.; Sauthoff, G. Structure and stability of Laves phases. Part I. Critical assessment of factors controlling Laves phase stability. *Intermetallics* **2004**, *12*, 713–720. [[CrossRef](#)]
20. Young, K.; Ouchi, T.; Yang, J.; Fetcenko, M.A. Studies of off-stoichiometric  $\text{AB}_2$  metal hydride alloy: Part 1. Structural characteristics. *Int. J. Hydrogen Energy* **2011**, *36*, 11137–11145. [[CrossRef](#)]
21. Liu, C.T.; Zhu, J.H.; Brady, M.P.; McKamey, C.G.; Pike, L.M. Physical metallurgy and mechanical properties of transition-metal Laves phase alloys. *Intermetallics* **2000**, *8*, 1119–1129. [[CrossRef](#)]
22. Johnston, R.L.; Hoffmann, R. Structure-bonding relationships in the Laves phases. *Z. Anorg. Allg. Chem.* **1992**, *616*, 105–120. [[CrossRef](#)]
23. Wong, D.F.; Young, K.; Ng, K.Y.S. First-principles study of structure, initial lattice expansion, and pressure-composition-temperature hysteresis for substituted  $\text{LaNi}_5$  and  $\text{TiMn}_2$  alloys. *Model. Simul. Mater. Sci. Eng.* **2016**, *24*, 085007. [[CrossRef](#)]
24. Nei, J.; Young, K.; Salley, S.O.; Ng, K.Y.S. Determination of C14/C15 phase abundance in Laves phase alloys. *Mater. Chem. Phys.* **2012**, *135*, 520–527. [[CrossRef](#)]
25. Shaltiel, D.; Jacob, I.; Davidov, D. Hydrogen absorption and desorption properties of  $\text{AB}_2$  Laves-phase pseudobinary compounds. *J. Less-Common Met.* **1977**, *53*, 117–131. [[CrossRef](#)]
26. Sapru, K.; Hong, K.; Fetcenko, M.A.; Venkatesan, S. Hydrogen storage materials and methods of sizing and preparing the same for electrochemical applications. U.S. Patent 4551400, 5 November 1985.
27. Zhu, J.H.; Liaw, P.K.; Liu, C.T. Effect of electron concentration on the phase stability of  $\text{NbCr}_2$ -based Laves phase alloys. *Mater. Sci. Eng.* **1997**, *A239-240*, 260–264. [[CrossRef](#)]
28. Moriwaki, Y.; Gamo, T.; Seri, H.; Iwaki, T. Electrode characteristics of C15-type Laves phase alloys. *J. Less-Common Met.* **1991**, *172–174*, 1211–1218. [[CrossRef](#)]
29. Wakao, S.; Sawa, H.; Furukawa, J. Effects of partial substitution and anodic oxidation treatment of Zr-V-Ni alloys on electrochemical properties. *J. Less-Common Met.* **1991**, *172–174*, 1219–1226. [[CrossRef](#)]
30. Züttel, A.; Meli, F.; Schlapbach, L. Electrochemical and surface properties of  $\text{Zr}(\text{V}_x\text{Ni}_{1-x})_2$  alloys as hydrogen-absorbing electrodes in alkaline electrolyte. *J. Alloys Compd.* **1994**, *203*, 235–241. [[CrossRef](#)]
31. Züttel, A.; Meli, F.; Chartouni, D.; Schlapbach, L.; Lichtenberg, F.; Friedrich, B. Properties of  $\text{Zr}(\text{V}_{0.25}\text{Ni}_{0.75})_2$  metal hydride as active electrode material. *J. Alloys Compd.* **1996**, *239*, 175–182. [[CrossRef](#)]
32. Yu, J.Y.; Lei, Y.Q.; Chen, C.P.; Wu, J.; Wang, Q.D. The electrochemical properties of hydrogen storage Zr-based Laves phase alloys. *J. Alloys Compd.* **1995**, *231*, 578–581. [[CrossRef](#)]
33. Gao, X.; Song, D.; Zhang, Y.; Zhou, Z.; Yang, H.; Zhang, W.; Shen, P.; Wang, M. Characteristics of the superstoichiometric C15-type Laves phase alloys and their hydride electrodes. *J. Alloys Compd.* **1995**, *231*, 582–586. [[CrossRef](#)]
34. Yoshida, M.; Ishibashi, H.; Susa, K.; Ogura, T.; Akiba, E. Crystal structure, hydrogen absorbing properties and electrode performances of Sc-based Laves phase alloys. *J. Alloys Compd.* **1995**, *226*, 161–165. [[CrossRef](#)]
35. Nakano, H.; Wakao, S. Substitution effect of elements in Zr-based alloys with Laves phase of nickel-hydride battery. *J. Alloys Compd.* **1995**, *231*, 587–593. [[CrossRef](#)]
36. Züttel, A.; Chartouni, D.; Gross, K.; Bächler, M.; Schlapbach, L. Structural- and hydriding-properties of the  $\text{Zr}(\text{V}_{0.25}\text{Ni}_{0.75})\alpha$  ( $1 \leq \alpha \leq 4$ ) alloys system. *J. Alloys Compd.* **1997**, *253–254*, 587–589. [[CrossRef](#)]

37. Sun, D.; Latroche, M.; Percheron-Guégan, A. Effects of lanthanum or cerium on the equilibrium of  $ZrNi_{1.2}Mn_{0.6}V_{0.2}Cr_{0.1}$  and its related hydrogenation properties. *J. Alloys Compd.* **1997**, *248*, 215–219. [[CrossRef](#)]
38. Kim, D.; Lee, S.; Jang, K.; Lee, J. The electrode characteristics of over-stoichiometric  $ZrMn_{0.5}V_{0.5}Ni_{1.4+y}$  ( $y = 0.0, 0.2, 0.4$  and  $0.6$ ) alloys with C15 Laves phase structure. *J. Alloys Compd.* **1998**, *268*, 241–247. [[CrossRef](#)]
39. Kim, D.; Lee, S.; Jung, J.; Jang, K.; Lee, J. Electrochemical properties of over-stoichiometric  $ZrMn_{1-x}V_xNi_{1.4+y}$  alloys with C15 Laves phase. *J. Electrochem. Soc.* **1998**, *145*, 93–98. [[CrossRef](#)]
40. Knosp, B.; Jordy, C.; Blanchard, P.; Berlureau, T. Evaluation of  $Zr(Ni, Mn)_2$  Laves phase alloys as negative active material for Ni-MH electric vehicle batteries. *J. Electrochem. Soc.* **1998**, *145*, 1478–1482. [[CrossRef](#)]
41. Knosp, B.; Vallet, L.; Blanchard, P. Performance of an  $AB_2$  alloy in sealed Ni-MH batteries for electric vehicles: quantification of corrosion rate and consequences on the battery performance. *J. Alloys Compd.* **1999**, *293*–*295*, 770–774. [[CrossRef](#)]
42. Lupu, D.; Biris, A.R.; Indrea, E.; Biris, A.S.; Nele, G.; Schlapbach, L.; Zuttle, A. Hydrogen absorption and hydride electrode behaviour of the Laves phase  $ZrV_{1.5-x}Cr_xNi_{1.5}$ . *J. Alloys Compd.* **1999**, *291*, 289–294. [[CrossRef](#)]
43. Chen, L.; Wu, F.; Tong, M.; Chen, D.M.; Long, R.B.; Shang, Z.Q.; Liu, H.; Sun, W.S.; Yang, K.; Wang, L.B.; et al. Advanced nanocrystalline Zr-based  $AB_2$  hydrogen storage electrode materials for NiMH EV batteries. *J. Alloys Compd.* **1999**, *293*–*295*, 508–520. [[CrossRef](#)]
44. Yang, X.G.; Zhang, W.K.; Lei, Y.Q.; Wang, Q.D. Electrochemical properties of Zr-V-Ni system hydrogen storage alloys. *J. Electrochem. Soc.* **1999**, *146*, 1245–1250. [[CrossRef](#)]
45. Gao, X.; Sun, X.; Toyoda, E.; Higuchi, H.; Nakagima, T.; Suda, S. Deterioration of Laves phase alloy electrode during cycling. *J. Power Sources* **1999**, *833*, 100–107. [[CrossRef](#)]
46. Lupu, D.; Biris, A.S.; Biris, A.R.; Mişan, I.; Indrea, E. Hydrogen absorption and electrode properties of  $Zr_{1-x}Ti_xV_{1.2}Cr_{0.3}Ni_{1.5}$  Laves phases. *J. Alloys Compd.* **2000**, *312*, 302–306. [[CrossRef](#)]
47. Hsu, Y.; Chiou, S.; Peng, T. Electrochemical hydrogenation behavior of C15-type  $Zr(Mn, Ni)_2$  alloy electrode. *J. Alloys Compd.* **2000**, *313*, 263–268. [[CrossRef](#)]
48. Zhang, H.; Lei, Y.; Li, D. Electrochemical performance of  $ZrMn_{0.5}V_{0.4}Ni_{1.1}Co_x$  Laves phase alloy electrode. *J. Power Sources* **2001**, *99*, 48–53. [[CrossRef](#)]
49. Cao, J.; Gao, X.; Lin, D.; Zhou, X.; Yuan, H.; Song, D.; Shen, P. Activation behavior of the Zr-based Laves phase alloy electrode. *J. Power Sources* **2001**, *93*, 141–144.
50. Yang, K.; Chen, D.; Chen, L.; Guo, Z.X. Microstructure, electrochemical performance and gas-phase hydrogen storage property of  $Zr_{0.9}Ti_{0.1}[(Ni,V,Mn)_{0.95}Co_{0.05}]_\alpha$  Laves phase alloys. *J. Alloys Compd.* **2002**, *333*, 184–189. [[CrossRef](#)]
51. Liu, H.; Li, R. Effect of Sn content on properties of  $AB_2$  hydrogen storage alloy. *Foundry Tech.* **2006**, *27*, 503–505. (In Chinese)
52. Huot, J.; Akiba, E.; Ogura, T.; Ishido, Y. Crystal structure, phase abundance and electrode performance of Laves phase compounds  $(Zr, A)V_{0.5}Ni_{1.1}Mn_{0.2}Fe_{0.2}$  ( $A \equiv Ti, Nb$  or  $Hf$ ). *J. Alloys Compd.* **1995**, *218*, 101–109. [[CrossRef](#)]
53. Joubert, J.; Latroche, M.; Percheron-Guégan, A.; Bouet, J. Improvement of the electrochemical activity of Zr-Ni-Cr Laves phase hydride electrode by secondary phase precipitation. *J. Alloys Compd.* **1996**, *240*, 219–228. [[CrossRef](#)]
54. Nakano, H.; Wakao, S.; Shimizu, T. Correlation between crystal structure and electrochemical properties of C14 Laves-phase alloys. *J. Alloys Compd.* **1997**, *253*–*254*, 609–612. [[CrossRef](#)]
55. Zhang, Q.A.; Lei, Y.Q.; Yang, X.G.; Ren, K.; Wang, Q.D. Annealing treatment of  $AB_2$ -type hydrogen storage alloys: II. Electrochemical properties. *J. Alloys Compd.* **1999**, *292*, 241–246. [[CrossRef](#)]
56. Song, X.; Zhang, X.; Leo, Y.; Wang, Q. Effect of microstructure on the properties of Zr-Mn-V-Ni  $AB_2$  type hydride electrode alloys. *Int. J. Hydrogen Energy* **1999**, *24*, 455–459. [[CrossRef](#)]
57. Du, Y.L.; Yang, X.G.; Zhang, Q.A.; Lei, Y.Q.; Zhang, M.S. Phase structures and electrochemical properties of the Laves phase hydrogen storage alloys  $Zr_{1-x}Ti_x(Ni_{0.6}Mn_{0.3}V_{0.1}Cr_{0.05})_2$ . *Int. J. Hydrogen Energy* **2001**, *26*, 333–337. [[CrossRef](#)]
58. Iosub, V.; Joubert, J.; Latroche, M.; Cerny, R.; Percheron-Guegan, A. Hydrogen cycling induced diffraction peak broadening in C14 and C15 Laves phases. *J. Solid State Chem.* **2005**, *178*, 1799–1806. [[CrossRef](#)]

59. Banerjee, S.; Kumar, A.; Pillai, C.G.S. Improvement on the hydrogen storage properties of ZrFe<sub>2</sub> Laves phase alloy by vanadium substitution. *Intermetallics* **2014**, *51*, 30–36. [CrossRef]
60. Wu, T.; Xue, X.; Zhang, T.; Hu, R.; Kou, H.; Li, J. Microstructures and hydrogenation properties of (ZrTi)(V<sub>1-x</sub>Al<sub>x</sub>)<sub>2</sub> Laves phase intermetallic compounds. *J. Alloys Compd.* **2015**, *645*, 358–368. [CrossRef]
61. Young, K.; Ouchi, T.; Huang, B.; Chao, B.; Fetcenko, M.A.; Bendersky, L.A.; Wang, K.; Chiu, C. The correlation of C14/C15 phase abundance and electrochemical properties in the AB<sub>2</sub> alloys. *J. Alloys Compd.* **2010**, *506*, 841–848. [CrossRef]
62. Young, K.; Nei, J.; Ouchi, T.; Fetcenko, M.A. Phase abundances in AB<sub>2</sub> metal hydride alloys and their correlations to various properties. *J. Alloys Compd.* **2011**, *509*, 2277–2284. [CrossRef]
63. Young, K.; Ouchi, T.; Lin, X.; Reichman, B. Effects of Zn-addition to C14 metal hydride alloys and comparisons to Si, Fe, Cu, Y, and Mo-additives. *J. Alloys Compd.* **2016**, *655*, 50–59. [CrossRef]
64. Young, K.; Ouchi, T.; Huang, B.; Reichman, B.; Fetcenko, M.A. Studies of copper as a modifier in C14-predominant AB<sub>2</sub> metal hydride alloys. *J. Power Sources* **2012**, *204*, 205–212. [CrossRef]
65. Young, K.; Ouchi, T.; Huang, B.; Reichman, B.; Fetcenko, M.A. The structure, hydrogen storage, and electrochemical properties of Fe-doped C14-predominating AB<sub>2</sub> metal hydride alloys. *Int. J. Hydrogen Energy* **2011**, *36*, 12296–12304. [CrossRef]
66. Young, K.; Ouchi, T.; Huang, B.; Reichman, B. Effect of molybdenum content on structural, gaseous storage, and electrochemical properties of C14-predominant AB<sub>2</sub> metal hydride alloys. *J. Power Sources* **2011**, *196*, 8815–8825. [CrossRef]
67. Yartys, V.A. Ti-Zr Based AB<sub>2</sub> Alloys for High Power Metal Hydride Batteries. In Proceedings of the 15th International Symposium on Metal-Hydrogen System, Interlaken, Switzerland, 7–12 August 2016.
68. Wan, C.; Ju, X.; Wang, Y. EXAFS characterization of TiVCrMn hydrogen storage alloy upon hydrogen absorption-desorption cycles. *Int. J. Hydrogen Energy* **2012**, *37*, 990–994. [CrossRef]
69. Kim, S.R.; Lee, J.Y. Activation behaviour of ZrCrNiM<sub>0.05</sub> metal hydride electrodes (M = La, Mm (misch metal), Nd). *J. Alloys Compd.* **1992**, *185*, L1–L4. [CrossRef]
70. Young, K.; Wong, D.F.; Ouchi, T.; Huang, B.; Reichman, B. Effects of La-addition to the structure, hydrogen storage and electrochemical properties of C14 metal hydride alloys. *Electrochim. Acta* **2015**, *174*, 815–825. [CrossRef]
71. Visintin, A.; Peretti, A.A.; Fruiz, F.; Corso, H.L.; Triaca, W.E. Effect of additional catalytic phases imposed by sintering on the hydrogen absorption behavior of AB<sub>2</sub> type Zr-based alloys. *J. Alloys Compd.* **2007**, *428*, 244–251. [CrossRef]
72. Zhang, W.K.; Ma, C.A.; Yang, X.G.; Lei, Y.Q.; Wang, Q.D.; Lu, G.L. Influences of annealing heat treatment on phase structure and electrochemical properties of Zr(MnVNi)<sub>2</sub> hydrogen storage alloys. *J. Alloys Compd.* **1999**, *293–295*, 691–697. [CrossRef]
73. Rennert, P.; Radwan, A.M. Structural investigation of the Laves phase MgZn<sub>2</sub> with model potential calculations. *Physica Status Solidi (b)* **1977**, *79*, 167–173. [CrossRef]
74. Liu, Y.; Young, K. Microstructure investigation on metal hydride alloys by electron backscatter diffraction technique. *Batteries* **2016**, *2*. [CrossRef]
75. Young, K.; Ouchi, T.; Banik, A.; Koch, J.; Fetcenko, M.A. Improvement in the electrochemical properties of gas atomized AB<sub>2</sub> metal hydride alloys by hydrogen annealing. *Int. J. Hydrogen Energy* **2011**, *36*, 3547–3555. [CrossRef]
76. Boettinger, W.J.; Newbury, D.E.; Wang, K.; Bendersky, L.A.; Chiu, C.; Kattner, U.R.; Young, K.; Chao, B. Examination of multiphase (Zr, Ti)(V, Cr, Mn, Ni)<sub>2</sub> Ni-MH electrode alloys: Part I. Dendritic solidification structure. *Metall. Mater. Trans. A* **2010**, *41*, 2033–2047. [CrossRef]
77. Bendersky, L.A.; Wang, K.; Boettinger, W.J.; Newbury, D.E.; Young, K.; Chao, B. Examination of multiphase (Zr, Ti)(V, Cr, Mn, Ni)<sub>2</sub> Ni-MH electrode alloys: Part II. Solid-state transformation of the interdendritic B2 phase. *Metall. Mater. Trans. A* **2010**, *41*, 1891–1906. [CrossRef]
78. Young, K.H.; Fetcenko, M.A.; Ovshinsky, S.R.; Ouchi, T.; Reichman, B.; Mays, W. Improved surface catalysis of Zr-based Laves phase alloys for NiMH Batteries. In *Hydrogen at Surface and Interface*; Jerkiewicz, G., Feliu, J.M., Popov, B.N., Eds.; The Electrochemical Society, Inc.: New Jersey, USA, 2000; Volume 2000-16, pp. 59–71.

79. Young, K.; Regmi, R.; Lawes, G.; Ouchi, T.; Reichman, B.; Fetcenko, M.A.; Wu, A. Effects of aluminum substitution in C14-rich multi-component alloys for NiMH battery applications. *J. Alloys Compd.* **2010**, *490*, 282–292. [[CrossRef](#)]
80. Young, K.; Fetcenko, M.A.; Ouchi, T.; Li, F.; Koch, J. Effect of Sn-substitution in C14 Laves phase alloys for NiMH battery application. *J. Alloys Compd.* **2009**, *469*, 406–416. [[CrossRef](#)]
81. Young, K.; Ouchi, T.; Reichman, B.; Mays, W.; Regmi, R.; Lawes, G.; Fetcenko, M.A.; Wu, A. Optimization of Co-content in C14 Laves phase multi-component alloys for NiMH battery application. *J. Alloys Compd.* **2010**, *489*, 202–210. [[CrossRef](#)]
82. Young, K.; Ouchi, T.; Huang, B.; Reichman, B.; Blankenship, R. Improvement in -40 °C electrochemical properties of AB<sub>2</sub> metal hydride alloy in silicon incorporation. *J. Alloys Compd.* **2013**, *575*, 65–72. [[CrossRef](#)]
83. Young, K.; Young, M.; Ouchi, T.; Reichman, B.; Fetcenko, M.A. Improvement in high-rate dischargeability, activation, and low-temperature performance in multi-phase AB<sub>2</sub> alloys by partial substitution of Zr with Y. *J. Power Sources* **2012**, *215*, 279–287. [[CrossRef](#)]
84. Young, K.; Fetcenko, M.A.; Koch, J.; Morii, K.; Shimizu, T. Studies of Sn, Co, Al, and Fe additives in C14/C15 Laves alloys for NiMH battery application by orthogonal arrays. *J. Alloys Compd.* **2009**, *486*, 559–569. [[CrossRef](#)]
85. Young, K.; Huang, B.; Ouchi, T. Studies of Co, Al, and Mn substitutions in NdNi<sub>5</sub> metal hydride alloys. *J. Alloys Compd.* **2012**, *543*, 90–98. [[CrossRef](#)]
86. Young, K.; Ouchi, T.; Huang, B. Effects of various annealing conditions on (Nd, Mg, Zr)(Ni, Al, Co)<sub>3.74</sub> metal hydride alloys. *J. Power Sources* **2014**, *248*, 147–153. [[CrossRef](#)]
87. Young, K.; Ouchi, T.; Huang, B.; Nei, J. Structure, hydrogen storage, and electrochemical properties of body-centered-cubic Ti<sub>40</sub>V<sub>30</sub>Cr<sub>15</sub>Mn<sub>13</sub>X<sub>2</sub> alloys (X = B, Si, Mn, Ni, Zr, Nb, Mo, and La). *Batteries* **2015**, *1*, 74–90. [[CrossRef](#)]
88. Wong, D.F.; Young, K.; Nei, J.; Wang, L.; Ng, K.Y.S. Effects of Nd-addition on the structural, hydrogen storage, and electrochemical properties of C14 metal hydride alloys. *J. Alloys Compd.* **2015**, *647*, 507–518. [[CrossRef](#)]
89. Young, K.; Ouchi, T.; Meng, T.; Wong, D.F. Studies on the synergetic effects in multi-phase metal hydride alloys. *Batteries* **2016**, *2*. [[CrossRef](#)]
90. Mosavati, N.; Young, K.; Meng, T.; Ng, K.Y.S. Electrochemical open-circuit voltage and pressure-concentration-temperature isotherm comparison for metal hydride alloys. *Batteries* **2016**, *2*. [[CrossRef](#)]
91. Young, K.; Ouchi, T.; Fetcenko, M.A. Pressure-composition-temperature hysteresis in C14 Laves phase alloys: Part 1. Simple ternary alloys. *J. Alloys Compd.* **2009**, *480*, 428–433. [[CrossRef](#)]
92. Trapanese, M.; Franzitta, V.; Viola, A. Description of hysteresis of nickel metal hydride battery. In Proceedings of the 38th Annual Conference on IEEE Industrial Electronics Society, Montreal, QC, Canada, 25–28 October 2012; pp. 967–970.
93. Trapanese, M.; Franzitta, V.; Viola, A. Description of hysteresis in lithium battery by classical Preisach model. *Adv. Mater. Res.* **2013**, *622*, 1099–1103.
94. Trapanese, M.; Franzitta, V.; Viola, A. The Jiles Atherton model for description on hysteresis in lithium battery. In Proceedings of the Twenty-Eighth Annual IEEE Applied Power Electronics Conference and Exposition (APEC), Long Beach, CA, USA, 17–21 March 2013; pp. 2772–2775.
95. Schwarz, R.B.; Khachaturyan, A.G. Thermodynamics of open two-phase systems with coherent interface. *Phys. Rev. Lett.* **1995**, *74*, 2523–2526. [[CrossRef](#)]
96. Shen, H.T.; Young, K.H.; Meng, T.; Bendersky, L.A. Clean grain boundary found in C14/body-center-cubic multi-phase metal hydride alloys. *Batteries* **2016**, *2*. [[CrossRef](#)]
97. Lide, D.R. *CRC Handbook of Chemistry and Physics*, 74th ed.; CRC Press: Boca Raton, FL, USA, 1993; pp. 6–22.
98. Young, K.; Fetcenko, M.A.; Li, F.; Ouchi, T. Structural, thermodynamic, and electrochemical properties of Ti<sub>x</sub>Zr<sub>1-x</sub>(VNiCeMnCiAl)<sub>2</sub> C14 Laves phase alloys. *J. Alloys Compd.* **2008**, *464*, 238–247. [[CrossRef](#)]
99. Young, K.; Ouchi, T.; Fetcenko, M.A. Roles of Ni, Cr, Mn, Sn, Co, and Al in C14 Laves phase alloys for NiMH battery application. *J. Alloys Compd.* **2009**, *476*, 774–781. [[CrossRef](#)]
100. Young, K.; Ouchi, T.; Koch, J.; Fetcenko, M.A. Compositional optimization of vanadium-free hypo-stoichiometric AB<sub>2</sub> metal hydride alloy for Ni/MH battery application. *J. Alloys Compd.* **2012**, *510*, 97–106. [[CrossRef](#)]

101. Young, K.; Wong, D.F.; Nei, J. Effects of vanadium/nickel contents in Laves phase-related body-centered-cubic solid solution metal hydride alloys. *Batteries* **2015**, *1*, 34–53. [[CrossRef](#)]
102. Zheng, G.; Popov, B.N.; White, R.E. Electrochemical determination of the diffusion coefficient of hydrogen through an LaNi<sub>4.25</sub>Al<sub>0.75</sub> electrode in alkaline aqueous solution. *J. Electrochem. Soc.* **1995**, *142*, 2695–2698.
103. Notten, P.H.L.; Hokkeling, P. Double-phase hydride forming compounds: A new class of highly electrocatalytic materials. *J. Electrochem. Soc.* **1991**, *138*, 1877–1885. [[CrossRef](#)]
104. Young, K.; Nei, J. The current status of hydrogen storage alloy development for electrochemical applications. *Materials* **2013**, *6*, 4574–4608. [[CrossRef](#)]
105. Young, K.; Reichman, B.; Fetcenko, M.A. Electrochemical properties of AB<sub>2</sub> metal hydride alloys measured at –40 °C. *J. Alloys Compd.* **2013**, *580*, S349–S353. [[CrossRef](#)]
106. Young, K.; Huang, B.; Regmi, R.K.; Lawes, G.; Liu, Y. Comparisons of metallic clusters imbedded in the surface of AB<sub>2</sub>, AB<sub>5</sub>, and A<sub>2</sub>B<sub>7</sub> alloys. *J. Alloys Compd.* **2010**, *506*, 831–840. [[CrossRef](#)]



© 2017 by the authors. Licensee MDPI, Basel, Switzerland. This article is an open access article distributed under the terms and conditions of the Creative Commons Attribution (CC BY) license (<http://creativecommons.org/licenses/by/4.0/>).